



Jahn-Teller distortion driven ferromagnetism in a perovskite fluoride monolayerKe Ji ¹, Zongshuo Wu,¹ Xiaofan Shen,² Jianli Wang,¹ and Junting Zhang ^{1,*}¹*School of Materials Science and Physics, China University of Mining and Technology, Xuzhou 221116, China*²*National Laboratory of Solid State Microstructures and Physics School, Nanjing University, Nanjing 210093, China*

(Received 15 February 2023; accepted 18 April 2023; published 24 April 2023)

The Jahn-Teller distortion and the resulting orbital order usually cause some fascinating correlated electronic behaviors, and generally lead to antiferromagnetism in perovskite bulks. Here we demonstrate that the Jahn-Teller distortion present in the perovskite fluoride KCrF_3 bulk can be retained to the two-dimensional limit, resulting in a staggered orbital order and ferromagnetism in the perovskite monolayer. Octahedral tilt and rotation distortion also appear in the ground-state structure of the perovskite monolayer, which have minor effects on the electronic and magnetic properties with respect to the Jahn-Teller distortion. In addition, in the prototype phase without structural distortion, the partial occupation of the e_g orbitals leads to a ferromagnetic metallic state. This work facilitates the design of two-dimensional ferromagnets and functional properties based on Jahn-Teller distortion and orbital order.

DOI: [10.1103/PhysRevB.107.134431](https://doi.org/10.1103/PhysRevB.107.134431)**I. INTRODUCTION**

Two-dimensional (2D) ferromagnetism has attracted considerable interest due to the potential applications in next-generation spintronics devices with high density, high processing speed, and low-energy consumption [1–6]. However, the existence of 2D ferromagnetism was once a longstanding open question because the long-range magnetic order is prohibited at finite temperature in the 2D isotropic Heisenberg model according to the Mermin-Wagner theorem [7]. Until 2017, 2D ferromagnetism was first experimentally confirmed in the van der Waals materials CrI_3 and $\text{Cr}_2\text{Ge}_2\text{Te}_6$ [8,9]. Subsequently, many 2D ferromagnets have been discovered experimentally or proposed theoretically, however mostly focused on van der Waals materials [10–15].

Compared with van der Waals materials, perovskite materials exhibit more abundant correlated electronic behaviors, such as giant magnetoresistance, superconductivity, and magnetoelectric multiferroics, due to the competition and coupling between various degrees of freedom in lattice, charge, orbital, and spin [16–19]. However, unlike van der Waals materials that retain their structural and chemical bonding properties when reduced to a monolayer, 2D perovskites may undergo structural reconstruction with respect to their bulk phases due to the changes in ion coordination and chemical bonds. Therefore, whether some interesting phenomena found in perovskite bulks can exist in 2D perovskites remains a key issue to be solved. Recently, some stress-free perovskite monolayers have been experimentally prepared and can be transferred to any desired substrate [20–22]. These experimental advances not only provide great opportunities for the theoretical design of functional properties based on 2D perovskites such as ferroelectricity, ferromagnetism, and multiferroics [23–27], but also for the experimental realization of a perovskite moiré

superlattice via rotational misalignment and heterobilayers with different lattice constants [28,29].

Jahn-Teller (JT) distortion, as a common type of lattice distortion in perovskites, is usually associated with the breaking of the electron degeneracy of the transition-metal ions [30]. In general, the JT distortion is accompanied by the appearance of orbital order. The most typical example is the perovskite rare-earth manganite, as a representative material of the giant magnetoresistance effect [16]. The cooperative JT distortion leads to an in-plane staggered orbital order, which is responsible for its rich magnetic phases [31–33]. Another typical example is perovskite halide containing JT-active ions, such as Cr^{2+} or Cu^{2+} ions. The staggered orbital order tends to form an in-plane ferromagnetic order, whereas the interplane antiferromagnetic coupling causes these materials to exhibit antiferromagnetism, i.e., *A*-type antiferromagnetic order [34–37]. It can be expected that 2D ferromagnetism may occur in the monolayers of these perovskites if the JT distortion and the staggered orbital order can be maintained to the monolayer limit.

In this paper, we focus on a perovskite fluoride monolayer with complete octahedra (formula K_2CrF_4) and study its lattice dynamics, structural, electronic, and magnetic properties through first-principles calculations. Our results show that only the JT distortion is a dynamically unstable mode, whereas the ground-state structure exhibits octahedral tilt and rotation distortion in addition to the JT distortion. The cooperative JT distortion leads to a staggered orbital order and opens an indirect band gap in the ground-state phase. Ferromagnetism is dominated by strong ferromagnetic coupling of the nearest-neighbor (NN) exchange interaction, and can exist even in the prototype phase without JT distortion and orbital order.

II. COMPUTATIONAL DETAILS

The first-principles calculations based on density functional theory (DFT) were performed using the

*juntingzhang@cumt.edu.cn

projector-augmented wave (PAW) method [38], as implemented in the Vienna *ab initio* simulation package (VASP) [39]. The Perdew-Burke-Ernzerhof functional modified for solids (PBEsol) [40] was used as the exchange-correlation functional. Electron correlation was treated using the Hubbard- U method within the rotationally invariant formalism [41,42] and an effective value of $U_{\text{eff}} = 1.5$ eV for the Cr $3d$ states was determined by self-consistent calculation based on the constrained random-phase approximate method [43]. Due to the periodic condition, a vacuum space of 20 Å was utilized to keep adjacent images apart in the vertical direction. A plane-wave cutoff energy of 600 eV was used for the plane-wave expansion, and a Γ -centered $9 \times 9 \times 1$ k -point mesh was used for the Brillouin zone integration. The electronic self-consistent loop was performed at the convergence threshold of 10^{-6} eV. The in-plane lattice constants and internal atomic coordinates were relaxed until the Hellman-Feynman force on each atom was less than 10^{-2} eV/Å.

The ISOTROPY tool [44] was used to aid with the group-theoretical analysis. Phonon band structures were calculated using density functional perturbation theory (DFPT). The phonon frequencies and corresponding eigenmodes were calculated on the basis of the extracted force-constant matrices, as implemented in the PHONOPY code [45]. The Nosé heat bath scheme was employed to carry out the first-principles molecular dynamics simulations in a canonical ensemble. A large supercell of $3 \times 3 \times 1$ was used to minimize the constraint of periodic boundary conditions. The magnetic exchange interaction parameters were calculated using the Green's function method with the local rigid spin rotation treated as a perturbation, as implemented in the TB2J package [46]. The Monte Carlo simulations were performed to verify the magnetic ground state and estimate the magnetic transition temperature. A 32×32 supercell with periodic boundary condition and the annealing algorithm were used in simulations.

III. RESULTS AND DISCUSSION

A. Lattice dynamics

Considering the possible structural reconstruction when reduced to 2D, we start from the prototype phase of the perovskite monolayer (space group $P4/mmm$). Besides JT distortion, octahedral rotation is another common type of structural distortion that may occur in 2D perovskites. Octahedral rotation distortion is caused by cationic radius mismatch and is therefore very common in perovskites [30]. In 2D perovskites, it can be divided into a rotation mode belonging to irreducible representation M_2^+ and a tilt mode belonging to irreducible representation M_5^+ , corresponding to the rotation of the octahedron around the out-of-plane and in-plane axes, respectively, as shown in Fig. 1(a). The JT distortion can be divided into JT_1 and JT_2 modes, corresponding to the irreducible representations M_3^+ and M_4^+ , respectively. The JT_1 mode represents the elongation of two in-plane bonds and the shortening of the other two in-plane bonds in a single octahedron, while the JT_2 mode refers to the elongation of the two out-of-plane bonds and the contraction of the four in-plane bonds, as shown in Fig. 1(a).

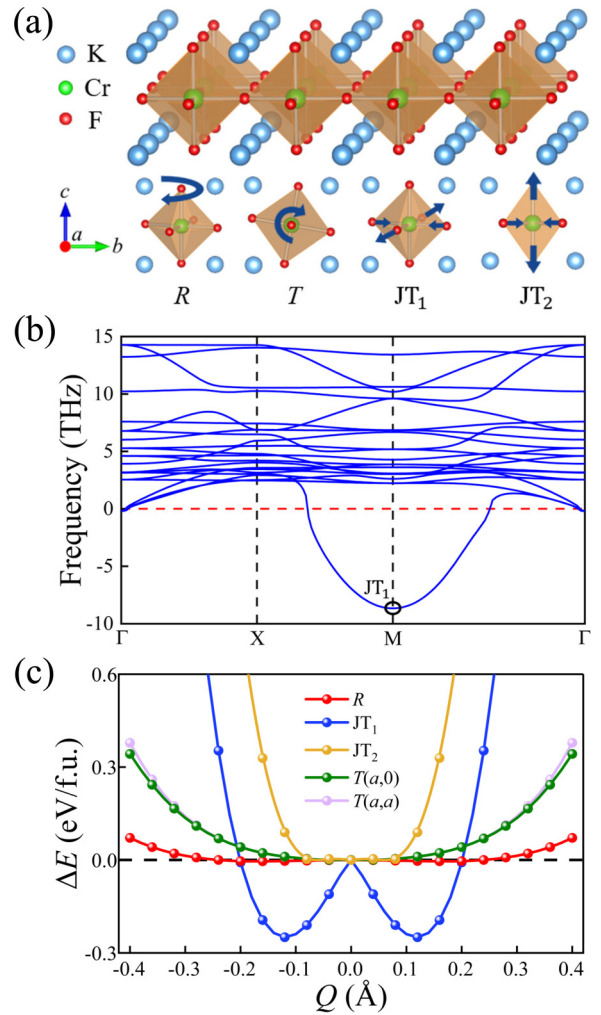


FIG. 1. (a) Crystal structure of the prototype phase of the perovskite monolayer and schematic diagram of the four octahedral distortion modes: rotation (R), tilt (T), JT_1 , and JT_2 . Curved arrows represent the direction of rotation of the octahedron. Straight arrows represent the direction of anion displacement due to JT distortion. (b) Phonon spectrum of the prototype phase of the K_2CrF_4 monolayer. The lowest-frequency soft mode belongs to the JT_1 mode. (c) Change in energy as a function of the amplitude of each distortion mode for the prototype phase. Two special in-plane directions are considered for the rotation axis of the tilt mode.

We first calculated the phonon spectrum of the prototype phase, whose in-plane lattice constant is 4.13 Å after structural optimization. Figure 1(b) shows that an unstable vibrational mode (i.e., soft mode) occurs at the high-symmetry M point in the Brillouin zone, which belongs to the JT_1 mode. Then we calculated the energy gain caused by the freezing of each octahedral distortion mode. For the tilt mode with 2D irreducible representation, two different order parameters $M_5^+(a, 0)$ and $M_5^+(a, a)$ were considered, corresponding to the octahedral rotation axis along the [100] and [110] directions, respectively. The results show that both the tilt mode and the JT_2 mode show parabolic energy curves, i.e., no energy gain, while the rotation mode has a slight energy gain, as shown in Fig. 1(c). In contrast, the JT_1 mode shows a typical double-well energy curve, that is, its emergence can significantly

TABLE I. Symmetry and energy of structural phases resulting from the single distortion mode and their various combinations in the K_2CrF_4 monolayer. The symbol “-” indicates that the corresponding structural phase is unstable since it transforms into other structure phases after structural optimization.

Distortion modes	Space group	ΔE (meV/f.u.)
<i>Para</i>	$P4/mmm$ (No.123)	108
$R(M_2^+)$	$P4/mbm$ (No.127)	113
$T(a,0)(M_5^+)$	$Pmna$ (No.53)	109
$T(a,a)(M_5^+)$	$Cmma$ (No.67)	110
$JT_1(M_3^+)$	$P4/mbm$ (No.127)	31
$JT_2(M_4^+)$	$P4/mmm$ (No.123)	147
$R \oplus JT_1$	$Pbam$ (No.55)	32
$R \oplus JT_2$	$P4/m$ (No.83)	98
$R \oplus T(a,0)$	$P2_1/c$ (No.14)	0
$R \oplus T(a,a)$	$C2/m$ (No.12)	111
$T(a,0) \oplus JT_1$	$P2_1/c$ (No.14)	0
$T(a,0) \oplus JT_2$	$P2/m$ (No.10)	147
$T(a,a) \oplus JT_1$	$C2/m$ (No.12)	4
$T(a,a) \oplus JT_2$	$C2/m$ (No.12)	-
$R \oplus JT_1 \oplus T(a,0)$	$P2_1/c$ (No.14)	0
$R \oplus JT_1 \oplus T(a,a)$	$P\bar{1}$ (No.2)	-
$R \oplus JT_2 \oplus T(a,0)$	$P\bar{1}$ (No.2)	-
$R \oplus JT_2 \oplus T(a,a)$	$P\bar{1}$ (No.2)	-

reduce the energy of the system. These results imply the presence of JT_1 distortion in the ground-state structure.

B. Ground-state structure

In order to determine the ground-state structure of the K_2CrF_4 monolayer, we considered the structural phases caused by each distortion mode and their various combinations (see Table I). We analyzed the symmetry of all structural phases, and calculated their energy by optimizing the atomic coordinates and the in-plane lattice constants under fixed structural symmetry. Of all the structural phases caused by a single distortion mode, only the structural phase of the JT_1 mode has lower energy than the prototype phase. For some structural phases established by multiple distortion modes, some distortion modes such as JT_2 will disappear after structural optimization. Furthermore, some additional distortion modes allowed by symmetry may be introduced after structural optimization, such as in the lowest-energy $P2_1/c$ phase. This ground-state phase can be established by a combination of tilt mode with rotation or JT_1 mode. However, all three distortion modes appear in the ground-state structure, where the JT_1 and tilt mode have considerable amplitude while the rotation distortion is very slight. The octahedral distortion of the ground-state structure is similar to that of the bulk phase, which exhibits both the JT_1 and tilt distortion at low temperature [35,36]. In order to verify the stability of the ground-state structure, we further calculated its phonon spectrum [see Fig. 2(a)] and performed first-principles molecular dynamics simulations [see Fig. 2(b)], which confirm its dynamic stability and thermodynamic stability, respectively.

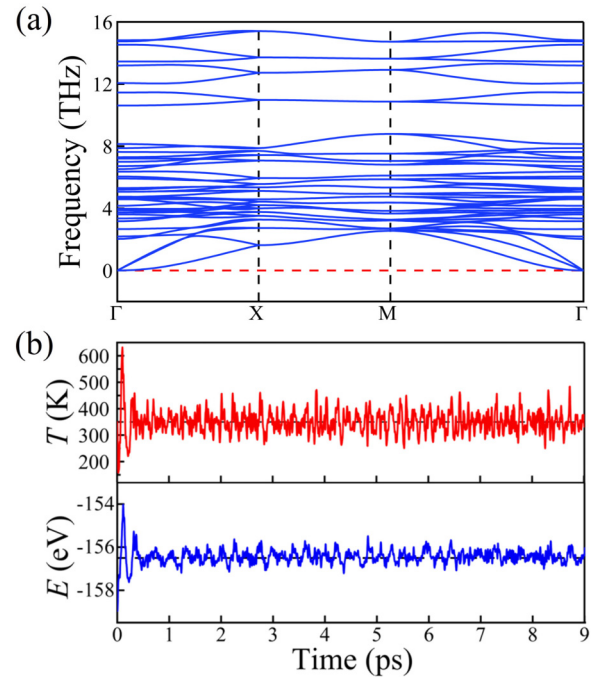


FIG. 2. (a) Phonon spectrum and (b) first-principles molecular dynamics simulations at 350 K of the ground-state phase.

C. Electronic property

In order to elucidate the effect of structural distortion on the electronic property of the K_2CrF_4 monolayer, we first calculated the projected band structure of the prototype phase [see Fig. 3(a)]. In 2D perovskite, the octahedral crystal field (O_h symmetry) transforms into the tetrahedral crystal field (D_{4h} symmetry), which causes the double-degenerate e_g orbitals to split into a lower-energy $d_{x^2-y^2}$ orbital and a higher-energy $d_{3z^2-r^2}$ orbital, and the triple-degenerate t_{2g} orbitals to split into the single d_{xy} orbital and the double-degenerate d_{xz}/d_{yz} orbitals. The electronic configuration of the Cr^{2+} ion is a high-spin state $t_{2g}^3 e_g^1$, i.e., the spin-up t_{2g} orbitals are fully occupied and the e_g orbitals are half-full occupied. In the prototype phase, the band formed by the $d_{x^2-y^2}$ orbital shows significant dispersion due to the large orbital overlap, as shown in Fig. 3(a). The two bands formed by the e_g orbitals have very close energy near the high-symmetry M point, which causes the Fermi level to cross these two bands, namely, exhibiting a metallic state.

In the ground-state phase, the cooperative JT_1 distortion causes the longest Cr-F bond to be staggered in the ab plane, which reduces the energy of the in-plane e_g orbitals ($d_{3x^2-r^2}$ and $d_{3y^2-r^2}$). In addition, the octahedral tilt distortion causes the Cr-F-Cr bond angle to deviate significantly from 180° . These structural distortions reduce the overlap of the in-plane e_g orbitals, resulting in the suppression of band dispersion, as shown in Fig. 3(b). The bands formed by the two e_g orbitals are completely separated in energy, i.e., an indirect band gap of about 0.73 eV is opened. We further investigated the effect of various distortion modes on the electronic property of the ground-state phase by reducing the amplitude of one distortion mode while keeping the amplitudes of other modes constant. The band gap basically does not change with the

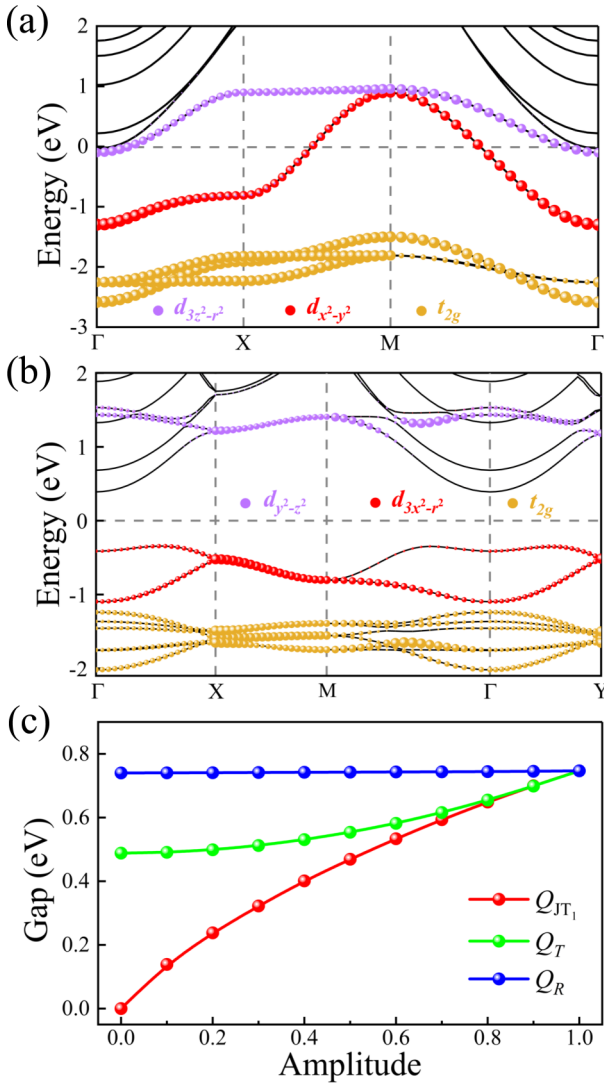


FIG. 3. The up-spin projected band structures of (a) the prototype and (b) the ground-state phases. The local z axis is along the out-of-plane direction, and the x axis is along the longest Cr-F bond. (c) Variation of band gap with the relative amplitude of each distortion mode in the ground-state phase.

weakening of the rotation mode due to its small amplitude, but reduces significantly with that of the tilt mode, as shown in Fig. 3(c). The band gap still exists even if the tilt distortion is completely removed. However, the band gap decreases more rapidly with the weakening of the JT_1 mode, and disappears when the JT_1 mode is completely removed. Therefore, the emergence of JT_1 distortion plays a key role in the insulating behavior of the ground-state phase, similar to the perovskite rare-earth manganites [31].

D. Magnetic property

Next we determined the magnetic ground state of the prototype phase. Magnetic structures with different periodic modulation are represented by the wave vector \mathbf{q} , whose general value represents the spiral spin order. For high-symmetry points, $\mathbf{q} = \Gamma$ corresponds to the ferromagnetic order, while

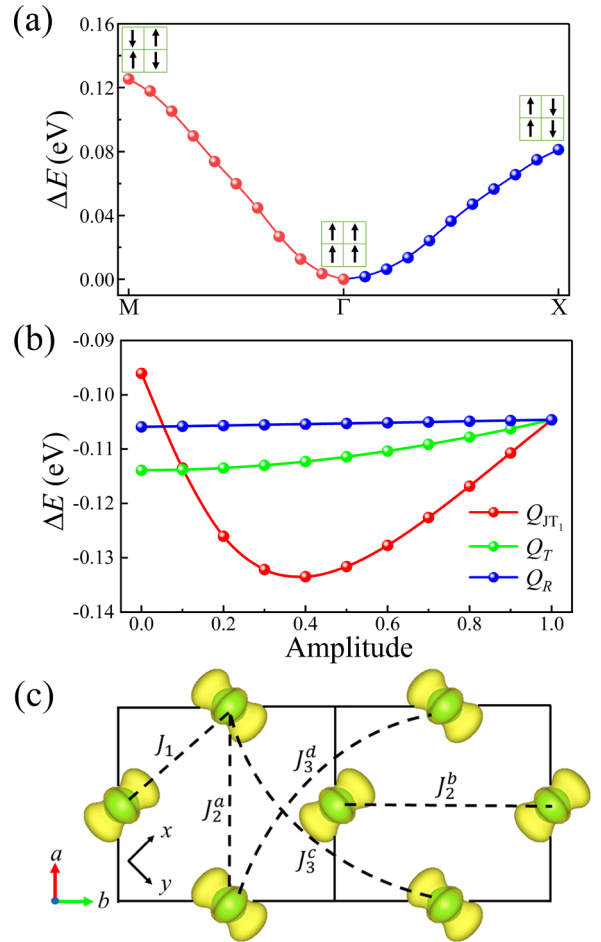


FIG. 4. (a) Energy of the magnetic ordering as a function of the spin spiral wave vector in the prototype phase. (b) Variation of energy difference between the ferromagnetic (FM) and the Néel antiferromagnetic (AFM) orders ($\Delta E = E_{\text{FM}} - E_{\text{AFM}}$) with the relative amplitude of each distortion mode in the ground-state phase. (c) The partial charge density at the valence band maximum and the considered exchange interactions in the ground-state phase.

$\mathbf{q} = M, X$ represent the collinear Néel and stripe antiferromagnetic orders, respectively. Figure 4(a) shows the variation of energy with the wave vector. The results show that the ferromagnetic order has the lowest energy, so the prototype phase exhibits a ferromagnetic metallic state. The origin of ferromagnetism of the prototype phase can be attributed to the double-exchange mechanism since the partial occupation of the two e_g orbitals resulting in the emergence of the itinerant electrons.

For the ground-state structure, the energy of the ferromagnetic order is still lower than that of the antiferromagnetic orders. To reveal the role of different distortion modes in the emergence of ferromagnetism, we varied the amplitudes of the three distortion modes in the ground-state phase, and then calculated the variation of the energy difference between the ferromagnetic and the Néel antiferromagnetic orders with the amplitude of each mode. This energy difference actually represents the NN exchange interaction parameter. As shown in Fig. 4(b), the energy difference does not vary with the amplitude of the rotation mode, while the weakening of the

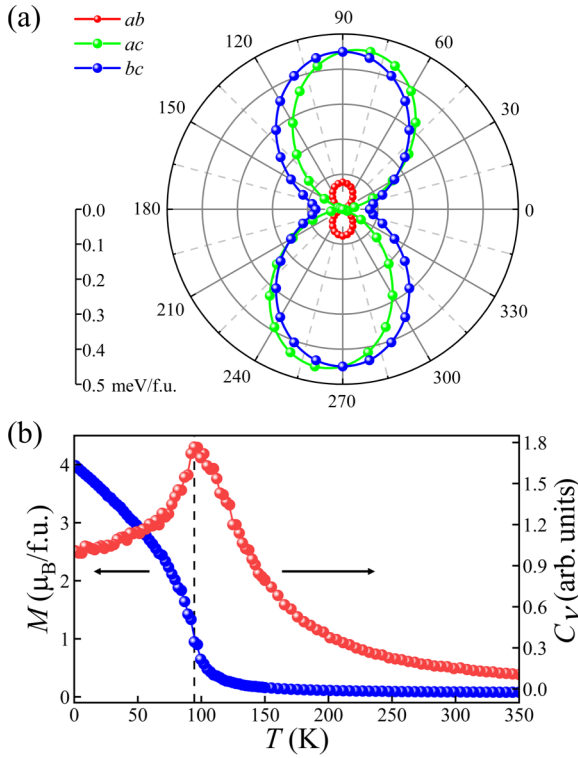


FIG. 5. (a) Magnetic anisotropy energy of the ground-state phase. The change in energy is shown as a function of the spin angle. When the spins lie in the ab (ac) and bc planes, the spin angle refers to the a and b axes, respectively. (b) Monte Carlo simulations of the ground-state phase. Magnetization (M) and specific heat (C_V) are shown as functions of temperature.

tilt mode leads to a slight decrease in the energy difference. In contrast, the energy difference varies significantly and non-monotonically with the amplitude of the JT_1 mode. The trend of ferromagnetism is first enhanced and then weakened with the increasing amplitude of the JT_1 mode. This non-monotonic change may result from the competition between the two interactions. Specifically, the JT_1 distortion induces the occurrence of the staggered orbital order [see Fig. 4(c)] that causes ferromagnetic superexchange interaction; however, its further enhancement will reduce the overlap of the occupied $d_{3x^2-r^2}/d_{3y^2-r^2}$ orbitals and thus weaken the superexchange interactions. The ferromagnetic order consistently has a lower energy throughout the varying range, indicating the robustness of the ferromagnetism.

Then we calculated the Heisenberg magnetic exchange interaction parameters by using the Green's function method based on magnetic force theorem. The NN, second-nearest-neighbor (SNN), and third-nearest-neighbor (TNN) exchange interactions are shown in Fig. 4(c). The SNN exchange interaction is split into two classes, J_2^a and J_2^b , due to the presence of the tilt distortion. Similarly, the orbital order causes the TNN exchange interaction to split into J_3^c and J_3^d . The NN exchange interaction results in a strong ferromagnetic coupling $J_1 = 11.75$ meV (with normalized spin moment), while the SNN exchange interaction is very weak, with values of $J_2^a = 0.36$ and $J_2^b = 0.22$ meV. The TNN exchange

interaction shows significant anisotropy, with a considerable antiferromagnetic coupling along the σ -bond direction ($J_3^c = -1.47$ meV), but very slight along the π -bond direction ($J_3^d = 0.02$ meV). For comparison, we recalculated the exchange interaction parameters using the four-state method [47], with $J_1 = 12.65$, $J_2^a = 0.81$, $J_2^b = 0.72$, $J_3^c = -1.21$, and $J_3^d = -0.62$ meV. The exchange interaction parameters calculated by both methods are quite close, except for the very weak exchange interactions. Therefore, the ferromagnetism of the ground-state phase is dominated by the NN ferromagnetic exchange interaction, which can be explained by the Goodenough-Kanamori-Anderson (GKA) rule in superexchange interaction. According to the GKA rule, the staggered orbital order leads to a ferromagnetic e_g - e_g exchange coupling, in addition to the ferromagnetic e_g - t_{2g} coupling. These ferromagnetic couplings are much stronger than the antiferromagnetic coupling between the t_{2g} - t_{2g} orbitals. These analyses are confirmed by the orbital decomposition of the magnetic exchange interaction. The ferromagnetic coupling of the NN exchange interaction mainly arises from the $d_{3x^2-r^2}$ - d_{xy} and $d_{3x^2-r^2}$ - $d_{3y^2-r^2}$ coupling, with values of 8.49 and 2.64 meV, respectively. Therefore, the orbital order plays an important role in the emergence of ferromagnetism of the ground-state phase.

The magnetic anisotropy calculation shows that the in-plane spin orientation has lower energy, while the tilt distortion causes a slight in-plane anisotropy, leading to the easy-magnetization axis along the tilt axis, as shown in Fig. 5(a). The magnetic anisotropy basically originates from the spin-orbit-coupling effect of Cr ion. The orbital magnetic moment of all ions is almost zero, while the spin magnetic moment is mainly concentrated on the Cr ion. Then, Monte Carlo simulations were performed to confirm the ferromagnetism and estimate the Curie temperature of the ground-state phase. The Heisenberg spin model containing the magnetic anisotropy energy term,

$$H = - \sum_{ij} J_{ij} \mathbf{S}_i \cdot \mathbf{S}_j - \sum_i A (\mathbf{S}_i^z)^2,$$

was used, where J_{ij} contains the NN, SNN, and TNN exchange parameters, A is the single-ion magnetic anisotropy constant, and \mathbf{S}_i^z represents the component of the spin along the easy-magnetization axis. As shown in Fig. 5(b), the ferromagnetism of the ground-state phase is further confirmed by the magnetization curve, and the Curie temperature is estimated to be 94 K according to the specific curve, slightly higher than the magnetic phase transition temperature of the bulk phase [36].

IV. CONCLUSION

In conclusion, we have systematically studied the lattice dynamics, structural, electronic, and magnetic properties of the perovskite monolayer K_2CrF_4 . Three lattice distortion modes appear in the ground-state structure: JT_1 distortion, octahedral tilt, and rotation distortion, of which the former has a significant effect on electronic and magnetic properties. The JT_1 distortion causes a staggered orbital order, resulting in a ferromagnetic semiconductor for the

ground-state phase. Both the ground-state and the prototype phases exhibit ferromagnetism, which is derived from the superexchange and double-exchange mechanisms, respectively. This work demonstrates that perovskite monolayers containing JT-active magnetic ions may provide a broad platform for designing 2D ferromagnets.

ACKNOWLEDGMENTS

This work was supported by the Fundamental Research Funds for the Central Universities (Grant No. 2019QNA30). Computer resources provided by the High Performance Computing Center of Nanjing University are gratefully acknowledged.

-
- [1] Z. Wang, I. Gutiérrez-Lezama, N. Ubrig, M. Kroner, M. Gibertini, T. Taniguchi, K. Watanabe, A. Imamoğlu, E. Giannini, and A. F. Morpurgo, Very large tunneling magnetoresistance in layered magnetic semiconductor CrI_3 , *Nat. Commun.* **9**, 2516 (2018).
- [2] T. C. Song, X. H. Cai, M. W.-Y. Tu, X. Zhang, B. Huang, N. P. Wilson, K. L. Seyler, L. Zhu, T. Taniguchi, K. Watanabe, M. A. McGuire, D. H. Cobden, D. Xiao, W. Yao, and X. D. Xu, Giant tunneling magnetoresistance in spin-filter van der Waals heterostructures, *Science* **360**, 1214 (2018).
- [3] D. R. Klein, D. MacNeill, J. L. Lado, D. Soriano, E. Navarro-Moratalla, K. Watanabe, T. Taniguchi, S. Manni, P. Canfield, J. Fernández-Rossier, and P. Jarillo-Herrero, Probing magnetism in 2D van der Waals crystalline insulators via electron tunneling, *Science* **360**, 1218 (2018).
- [4] H. H. Kim, B. Yang, T. Patel, F. Sfigakis, C. Li, S. Tian, H. Lei, and A. W. Tsen, One million percent tunnel magnetoresistance in a magnetic van der Waals heterostructure, *Nano Lett.* **18**, 4885 (2018).
- [5] C. Gong and X. Zhang, Two-dimensional magnetic crystals and emergent heterostructure devices, *Science* **363**, eaav4450 (2019).
- [6] X. Jiang, Q. X. Liu, J. P. Xing, N. S. Liu, Y. Guo, Z. F. Liu, and J. J. Zhao, Recent progress on 2D magnets: Fundamental mechanism, structural design and modification, *Appl. Phys. Rev.* **8**, 031305 (2021).
- [7] N. D. Mermin and H. Wagner, Absence of Ferromagnetism or Antiferromagnetism in One- or Two-Dimensional Isotropic Heisenberg Models, *Phys. Rev. Lett.* **17**, 1133 (1966).
- [8] C. Gong, L. Li, Z. L. Li, H. W. Ji, A. Stern, Y. Xia, T. Cao, W. Bao, C. Z. Wang, Y. Wang, Z. Q. Qiu, R. J. Cava, S. G. Louie, J. Xia, and X. Zhang, Discovery of intrinsic ferromagnetism in two-dimensional van der Waals crystals, *Nature (London)* **546**, 265 (2017).
- [9] B. Huang, G. Clark, E. Navarro-Moratalla, D. R. Klein, R. Cheng, K. L. Seyler, D. Zhong, E. Schmidgall, M. A. McGuire, D. H. Cobden, W. Yao, D. Xiao, P. Jarillo-Herrero, and X. Xu, Layer-dependent ferromagnetism in a van der Waals crystal down to the monolayer limit, *Nature (London)* **546**, 270 (2017).
- [10] M. Bonilla, S. Kolekar, Y. Ma, H. C. Diaz, V. Kalappattil, R. Das, T. Eggers, H. R. Gutierrez, M.-H. Phan, and M. Batzill, Strong room-temperature ferromagnetism in VSe_2 monolayers on van der Waals substrates, *Nat. Nanotechnol.* **13**, 289 (2018).
- [11] Y. J. Deng, Y. J. Yu, Y. C. Song, J. Z. Zhang, N. Z. Wang, Z. Y. Sun, Y. F. Yi, Y. Z. Wu, S. W. Wu, J. Y. Zhu, J. Wang, X. H. Chen, and Y. B. Zhang, Gate-tunable room-temperature ferromagnetism in two-dimensional Fe_3GeTe_2 , *Nature (London)* **563**, 94 (2018).
- [12] Y. Zhu, X. Kong, T. D. Rhone, and H. Guo, Systematic search for two-dimensional ferromagnetic materials, *Phys. Rev. Mater.* **2**, 081001(R) (2018).
- [13] M. Gibertini, M. Koperski, A. F. Morpurgo, and K. S. Novoselov, Magnetic 2D materials and heterostructures, *Nat. Nanotechnol.* **14**, 408 (2019).
- [14] C. Huang, J. Feng, F. Wu, D. Ahmed, B. Huang, H. Xiang, K. Deng, and E. Kan, Toward intrinsic room-temperature ferromagnetism in two-dimensional semiconductors, *J. Am. Chem. Soc.* **140**, 11519 (2018).
- [15] B. Wang, X. Zhang, Y. Zhang, S. Yuan, Y. Guo, S. Dong, and J. Wang, Prediction of a two-dimensional high- T_C -electron ferromagnetic semiconductor, *Mater. Horiz.* **7**, 1623 (2020).
- [16] E. Dagotto, T. Hotta, and A. Moreo, Colossal magnetoresistant materials: The key role of phase separation, *Phys. Rep.* **344**, 1 (2001).
- [17] E. Dagotto, Complexity in strongly correlated electronic systems, *Science* **309**, 257 (2005).
- [18] W. Eerenstein, N. D. Mathur, and J. F. Scott, Multiferroic and magnetoelectric materials, *Nature (London)* **442**, 759 (2006).
- [19] J. T. Zhang, Y. Zhou, F. Wang, X. F. Shen, J. L. Wang, and X. M. Lu, Coexistence and Coupling of Spin-Induced Ferroelectricity and Ferromagnetism in Perovskites, *Phys. Rev. Lett.* **129**, 117603 (2022).
- [20] D. Lu, D. J. Baek, S. S. Hong, L. F. Kourkoutis, Y. Hikita, and H. Y. Hwang, Synthesis of freestanding single-crystal perovskite films and heterostructures by etching of sacrificial water-soluble layers, *Nat. Mater.* **15**, 1255 (2016).
- [21] S. S. Hong, J. H. Yu, D. Lu, A. F. Marshall, Y. Hikita, Y. Cui, and H. Y. Hwang, Two-dimensional limit of crystalline order in perovskite membrane films, *Sci. Adv.* **3**, eaao5173 (2017).
- [22] D. X. Ji, S. H. Cai, T. R. Paudel, H. Y. Sun, C. C. Zhang, L. Han, Y. F. Wei, Y. P. Zang, M. Gu, Y. Zhang, W. P. Gao, H. X. Huyan, W. Guo, D. Wu, Z. B. Gu, E. Y. Tsymbal, P. Wang, Y. F. Nie, and X. Q. Pan, Freestanding crystalline oxide perovskites down to the monolayer limit, *Nature (London)* **570**, 87 (2019).
- [23] J. Lu, W. Luo, J. Feng, and H. Xiang, Unusual ferroelectricity in two-dimensional perovskite oxide thin films, *Nano Lett.* **18**, 595 (2018).
- [24] J. T. Zhang, X. Shen, Y. Wang, C. Ji, Y. Zhou, J. Wang, F. Huang, and X. Lu, Design of Two-Dimensional Multiferroics with Direct Polarization-Magnetization Coupling, *Phys. Rev. Lett.* **125**, 017601 (2020).
- [25] Y. Zhou, Z. Chen, Z. Wu, X. Shen, J. Wang, J. Zhang, and H. Sun, Hybrid improper ferroelectricity and magnetoelectric coupling in a two-dimensional perovskite oxide, *Phys. Rev. B* **103**, 224409 (2021).
- [26] Y. Zhou, S. Dong, C. Shan, K. Ji, and J. Zhang, Two-dimensional ferroelectricity induced by octahedral rotation

- distortion in perovskite oxides, *Phys. Rev. B* **105**, 075408 (2022).
- [27] X. Shen, F. Wang, X. Lu, and J. Zhang, Two-dimensional multiferroics with intrinsic magnetoelectric coupling in A-site ordered perovskite monolayers, *Nano Lett.* **23**, 735 (2023).
- [28] F. Jia, S. Xu, G. Zhao, C. Liu, and W. Ren, Structural and electronic properties of two-dimensional freestanding BaTiO₃/SrTiO₃ heterostructures, *Phys. Rev. B* **101**, 144106 (2020).
- [29] A. G. Ricciardulli, S. Yang, J. H. Smet, and M. Saliba, Emerging perovskite monolayers, *Nat. Mater.* **20**, 1325 (2021).
- [30] M. A. Carpenter and C. J. Howard, Symmetry rules and strain/order-parameter relationships for coupling between octahedral tilting and cooperative Jahn-Teller transitions in ABX₃ perovskites. I. Theory, *Acta Crystallogr. Sect. B: Struct. Sci.* **65**, 134 (2009).
- [31] T. Kimura, S. Ishihara, H. Shintani, T. Arima, K. T. Takahashi, K. Ishizaka, and Y. Tokura, Distorted perovskite with e_g^1 configuration as a frustrated spin system, *Phys. Rev. B* **68**, 060403(R) (2003).
- [32] J. T. Zhang, C. Ji, Y. Y. Shangguan, B. X. Guo, J. L. Wang, F. Z. Huang, X. M. Lu, and J. S. Zhu, Strain-driven magnetic phase transitions from an antiferromagnetic to a ferromagnetic state in perovskite RMnO₃ films, *Phys. Rev. B* **98**, 195133 (2018).
- [33] J. T. Zhang, C. Ji, J. L. Wang, W. S. Xia, X. M. Lu, and J. S. Zhu, Stabilization of E-type magnetic order caused by epitaxial strain in perovskite manganites, *Phys. Rev. B* **97**, 085124 (2018).
- [34] N. Binggeli and M. Altarelli, Orbital ordering, Jahn-Teller distortion, and resonant x-ray scattering in KCuF₃, *Phys. Rev. B* **70**, 085117 (2004).
- [35] S. Margadonna and G. Karotsis, Cooperative Jahn-Teller distortion, phase transitions, and weak ferromagnetism in the KCrF₃ perovskite, *J. Am. Chem. Soc.* **128**, 16436 (2006).
- [36] Y. Xiao, Y. Su, H.-F. Li, C. M. N. Kumar, R. Mittal, J. Persson, A. Senyshyn, K. Gross, and T. Brueckel, Neutron diffraction investigation of the crystal and magnetic structures in KCrF₃ perovskite, *Phys. Rev. B* **82**, 094437 (2010).
- [37] G. T. Wang, Z. Li, L. H. Zheng, and Z. X. Yang, First-principles study on the orbital ordering of KCrF₃, *Phys. Rev. B* **84**, 045111 (2011).
- [38] P. E. Blöchl, Projector augmented-wave method, *Phys. Rev. B* **50**, 17953 (1994).
- [39] G. Kresse and J. Furthmüller, Efficient iterative schemes for ab initio total-energy calculations using a plane-wave basis set, *Phys. Rev. B* **54**, 11169 (1996).
- [40] J. P. Perdew, A. Ruzsinszky, G. I. Csonka, O. A. Vydrov, G. E. Scuseria, L. A. Constantin, X. Zhou, and K. Burke, Erratum: Restoring the Density-Gradient Expansion for Exchange in Solids and Surfaces [Phys. Rev. Lett. 100, 136406 (2008)], *Phys. Rev. Lett.* **102**, 039902(E) (2009).
- [41] S. L. Dudarev, G. A. Botton, S. Y. Savrasov, C. J. Humphreys, and A. P. Sutton, Electron-energy-loss spectra and the structural stability of nickel oxide: An LSDA+*U* study, *Phys. Rev. B* **57**, 1505 (1998).
- [42] H. J. Kulik, M. Cococcioni, D. A. Scherlis, and N. Marzari, Density Functional Theory in Transition-Metal Chemistry: A Self-Consistent Hubbard *U* Approach, *Phys. Rev. Lett.* **97**, 103001 (2006).
- [43] E. Şaşıoğlu, C. Friedrich, and S. Blügel, Effective Coulomb interaction in transition metals from constrained random-phase approximation, *Phys. Rev. B* **83**, 121101(R) (2011).
- [44] B. J. Campbell, H. T. Stokes, D. E. Tanner, and D. M. Hatch, ISODISPLACE: A web-based tool for exploring structural distortions, *J. Appl. Crystallogr.* **39**, 607 (2006).
- [45] A. Togo and I. Tanaka, First principles phonon calculations in materials science, *Scr. Mater.* **108**, 1 (2015).
- [46] X. He, N. Helbig, M. J. Verstraete, and E. Bousquet, TB2J: A PYTHON package for computing magnetic interaction parameters, *Comput. Phys. Commun.* **264**, 107938 (2021).
- [47] H. J. Xiang, E. J. Kan, S.-H. Wei, M.-H. Whangbo, and X. G. Gong, Predicting the spin-lattice order of frustrated systems from first principles, *Phys. Rev. B* **84**, 224429 (2011).